

The Role of SST Structure in Convectively Coupled Kelvin–Rossby Waves and Its Implications for MJO Formation

IN-SIK KANG

School of Earth and Environmental Sciences, Seoul National University, Seoul, South Korea

FEI LIU

Department of Meteorology and International Pacific Research Center, University of Hawai'i at Mānoa, Honolulu, Hawaii

MIN-SEOP AHN

School of Earth and Environmental Sciences, Seoul National University, Seoul, South Korea

YOUNG-MIN YANG

Computational Science and Technology, Seoul National University, Seoul, South Korea

BIN WANG

Department of Meteorology and International Pacific Research Center, University of Hawai'i at Mānoa, Honolulu, Hawaii

(Manuscript received 11 May 2012, in final form 8 February 2013)

ABSTRACT

The dynamics of the Madden–Julian oscillation (MJO) are investigated using an aqua-planet general circulation model (GCM) and a simple one-and-a-half-layer model with a first-baroclinic mode and a planetary boundary layer. The aqua-planet GCM with zonally symmetric SST conditions simulates tropical intraseasonal disturbances with a dominant time scale of about 20 days, which is much faster than that of the observed MJO, although the GCM with realistic surface boundary conditions is shown to reproduce the observed MJO reasonably well. The SST with a broader meridional structure slows down the propagation speed. Several experiments done with various zonally symmetric surface boundary conditions showed that the meridional structure of the SST in fact is a control factor for the propagation characteristics of the MJO. With a simple theoretical model for the MJO, it is shown that the instability of the moist coupled Kelvin–Rossby waves depends on the SST structure, which determines the lower-level moisture field. The SST with a narrow meridional structure prefers to enhance only the fast eastward Kelvin wave, while the broader SST provides enough off-equatorial moisture for the growth of the Rossby component, which couples strongly with the Kelvin component and slows down the eastward modes. The SST influences the coupled Kelvin–Rossby waves through changes in the moist static stability of the free atmosphere and the frictional moisture convergence in the planetary boundary layer. The present results suggest that the essential dynamics of the MJO are rooted in a convectively coupled Kelvin–Rossby wave packet with frictional moisture convergence.

1. Introduction

Tropical intraseasonal variations are known to be largely controlled by the Madden–Julian oscillation (MJO; Madden and Julian 1971, 1972). A number of

studies have investigated the dynamical processes of the MJO and proposed various theories. Those theories can be referred to in reviews by Zhang (2005), Wang (2005), and Waliser (2006); however, there is yet no broadly agreed upon theory for the MJO. Although the theory has not been settled down, several GCMs have recently improved the MJO simulation by either improving or modifying the convective parameterization (Miura et al. 2007; Lee et al. 2008; Benedict and Randall 2009; Maloney 2009; Khouider et al. 2011; Kim and Kang

Corresponding author address: In-Sik Kang, School of Earth and Environmental Sciences, Seoul National University, Seoul 151-747, South Korea.
E-mail: kang@climate.snu.ac.kr

2012), giving the opportunity to test various existing theories (Kim et al. 2011). The aim of this study is to understand the dynamics of the MJO using both the GCM, which simulates the MJO reasonably well, and a simple dynamical model, which contains the fundamental dynamics of tropical circulation.

The MJO theories proposed so far include positive-only wave conditional instability of the second kind (CISK; Lau and Peng 1987; Hendon 1988), frictional moist Kelvin waves (Wang 1988), frictionally coupled moist Kelvin–Rossby wave packet (Wang and Rui 1990), wind–evaporation feedback (Emanuel 1987; Neelin et al. 1987), radiative–convective feedback (Hu and Randall 1994; Waliser 1996; Sobel and Gildor 2003), and air–sea interaction (Flatau et al. 1997; Wang and Xie 1998; Waliser et al. 1999; Hendon 2000). A detailed review can be seen in Wang (2005). More recently, several authors demonstrated the existence of the MJO mode by moisture coupling in a simple system where the moisture equation is explicitly treated (Majda and Stechmann 2009; Sobel and Maloney 2012). The multiscale interaction related to upscale transport effects from synoptic scales was also proposed as a possible dynamic of the MJO (Majda and Stechmann 2009; Wang and Liu 2011; Liu and Wang 2012, 2013; Liu et al. 2012). All of these theories provide some insight into the aspects and mechanisms of the MJO, but the fundamental physics of the MJO remain elusive.

Numerical simulation of the MJO has been a difficult task (Slingo et al. 1996; Waliser et al. 2003; Lin et al. 2006), although recent modeling studies have reported greater success in MJO simulation (Miura et al. 2007; Lee et al. 2008; Benedict and Randall 2009; Maloney 2009; Kim and Kang 2012). These successes are mainly related to improvements in convective parameterization. Several studies have shown that improvement of the MJO can be achieved by a simple modification of the existing convective parameterization (Lin et al. 2006; Lee et al. 2008; Bechtold et al. 2008; Chikira and Sugiyama 2010). The modifications have been made mainly by introducing triggering mechanisms of the convective parameterization in the GCM or better formulation of entrainment and detrainment in the convection schemes. However, not many attempts have been made to understand why such modifications of the convective parameterization improve the MJO. It has been speculated that the better simulation of the MJO is because of the enhancement of the interaction between the convection and large-scale circulation fields. However, the main reason why we do not understand the improvement may be related to our lack of understanding of key dynamical processes of the MJO.

Although, as mentioned above, there is yet no broadly agreed upon theory for the MJO, the interaction between

large-scale moisture dynamics and convection seems to be one of the key dynamical processes of the MJO (Wang 2005). In particular, the convectively coupled Kelvin wave proposed by Lau and Peng (1987) is able to explain several aspects of the observed MJO properties (Wheeler and Kiladis 1999), such as that of the eastward-propagating planetary-scale waves, although it is faster than that of the MJO. In the frictional wave CISK theory, the so-called moist coupled Kelvin–Rossby wave theory, friction in the planetary boundary layer (PBL) provides additional moisture convergence through surface friction and plays an essential role in coupling the moist Kelvin and Rossby wave modes (Wang and Rui 1990). This theory has been supported by several observational studies (Hendon and Salby 1994; Maloney and Hartmann 1998; Matthews 2000) and modeling studies (Sperber et al. 1997; Waliser et al. 1999; Lee et al. 2003). In the present study, we revisited this moist coupled Kelvin–Rossby wave theory to understand the MJO characteristics simulated by a GCM and to explain how the MJO characteristics are changed by different idealized conditions of the GCM.

This study was motivated by the results of Maloney et al. (2010), which examined the sensitivity of MJO simulation on SST structures (narrow and broad meridional structures) using a National Center for Atmospheric Research (NCAR) atmospheric general circulation model (AGCM) but with the convection scheme replaced by the relaxed Arakawa–Schubert scheme (RAS). They showed that the narrow SST, obtained by a zonal average of the observed SST, produces only weak eastward-propagating intraseasonal variability, but the broad SST, probably mimicking the western Pacific Ocean SST, produces a strong MJO-like feature, although it is very regular and the propagation speed is a little slower than the observed. We have tried to repeat their experiments with a different GCM, which has the capability of simulating a more observation-like MJO with a realistic land–sea contrast and SST conditions [shown in section 2 and Kim et al. (2009)] and found that the aqua-planet GCM produces tropical intraseasonal disturbances far different from those of the GCM with realistic SST conditions. In the past, the aqua-planet simulations have been carried out by a number of studies (Hayashi and Sumi 1986; Lee et al. 2003) examining the existence of the MJO in the GCM and/or the sensitivity of the simulated MJO on the physical parameters of the GCM. In an earlier study by Hayashi and Sumi (1986), their aqua-planet MJO was faster than in observations, and they ascribed this difference to model problems. However, the results by Maloney et al. (2010) show that the characteristics of the MJO were strongly controlled by the horizontal structure of the SST. Indeed, the simulations in the

present study with different meridional structures of SST produced different intraseasonal disturbances. The aim of the present study is to understand the differences—in other words, the role of the SST structure in the simulated MJO using a simple dynamical framework but containing basic moisture dynamics of the tropical atmosphere. The governing equation of the simple system is based on linearized shallow water equations with moisture physics and a frictional surface boundary layer, similar to that of Wang and Rui (1990).

Section 2 describes the GCM used in the present study and compares the simulated with the observed MJO. Section 3 describes the experimental settings of the aqua-planet experiments and shows the differences between the simulations using the aqua-planet GCM and the different meridional structures of the SST. In section 4, a simple analytical model is introduced to understand the governing dynamics of the MJO and to understand the role of the SST structure on the formation of the MJO. Summary and concluding remarks are given in section 5.

2. The model and simulated MJO

The model used here is an AGCM of Seoul National University (SNU). The dynamic core of the AGCM is based on the finite volume method developed at the Geophysical Fluid Dynamics Laboratory (GFDL) of Princeton University, with the horizontal resolution of approximately 300 km in the zonal direction (at the equator) and 300 km in the meridional direction. The model has 20 vertical levels in sigma coordinates. Most of the important atmospheric physics are included, such as deep and shallow cumulus convection, large-scale condensation, radiation, PBL processes, and gravity wave drag. The detailed description of the model can be found in Lee et al. (2001) and Kim and Kang (2012). This model has been used to understand and improve simulation of the MJO (Lee et al. 2001, 2003, 2008; Lin et al. 2006; Frierson et al. 2011; Kim et al. 2011). In particular, Lee et al. (2001) and Lin et al. (2006) examined the difference between MJOs simulated by the same SNU AGCM but with different convective parameterizations. They found that a triggering mechanism in the convection scheme plays a critical role in the realistic simulation of the MJO and that the Tokioka modification (Tokioka et al. 1988) is required to better simulate the MJO with a simplified version of the RAS (Moorthi and Suarez 1992), which is the deep convection scheme of the present AGCM. The Tokioka modification suppresses convective plumes with entrainment rates less than the threshold, which varies inversely with the PBL depth. The minimum threshold value is defined as $\mu_{\min} = a/D$, where D is the PBL depth and a is a nonnegative

constant. The value of $a = 0.1$ is sufficiently large that the Tokioka modification reduces light rains, which are much too frequent in the RAS scheme (a problem of the scheme), and intensifies and organizes the convective precipitation more effectively. The present AGCM used the value of $a = 0.075$. Another important parameter of the convection scheme in the present model, which affects the MJO simulation, is the e -folding time scale of the autoconversion precipitation process (Lee et al. 2001). This time scale is important in determining the intensity of the cloud–radiation interaction, which was proposed as one of the important mechanisms of intraseasonal disturbances (Hu and Randall 1994; Waliser 1996; Sobel and Gildor 2003; Fuchs and Raymond 2002; Stephens and Haynes 2007). The present model used a value of 2400 s for the autoconversion time scale. This SNU GCM was one of the climate models that the Climate Variability and Predictability (CLIVAR)/MJO working group used for application of their MJO simulation diagnostic to various climate models (see Kim et al. 2009).

To examine the model capability of the MJO simulation, the AGCM was integrated for 10 years, seasonally varying the observed SST conditions prescribed as boundary conditions of the model. The realistic land configuration and topography were also used in the model. Figure 1 shows the power spectrum of the 850-hPa zonal wind of the National Centers for Environmental Prediction (NCEP) reanalysis 1 data (Figs. 1a,c) and of the SNU AGCM data (Figs. 1b,d). Here, we used the NCEP 1 data for 7 years from 2002 to 2008 and the data are considered to be observations. In both the observations and the GCM (Figs. 1a,b), the maximum spectral power appears in the zonal wavenumber 1 and for a period of about 40 days. The GCM produces large spectral powers of wavenumber 1 on broader time scales than the observations. As done by Wheeler and Kiladis (1999), the zonal wavenumber–frequency spectra of the 15°N–15°S symmetric component of the 850-hPa zonal wind (U850) were made and are shown in Fig. 1c for the NCEP 1 data and in Fig. 1d for the SNU AGCM. Both figures show that the eastward-propagating waves are mostly represented by the Kelvin waves with different phase speeds, although the GCM phase speeds are somewhat faster than those of NCEP 1 for smaller-scale waves. In addition, large spectral power appears in zonal wavenumber 1 and in the wave period of 30–80 days in both figures. Westward-propagating waves also appear but are less organized.

The horizontal patterns of circulation and outgoing longwave radiation (OLR) anomalies associated with intraseasonal variations on time scales of 30–60 days are constructed for both observations and the model. Here, the normalized intraseasonal time series of OLR (NIOLR)

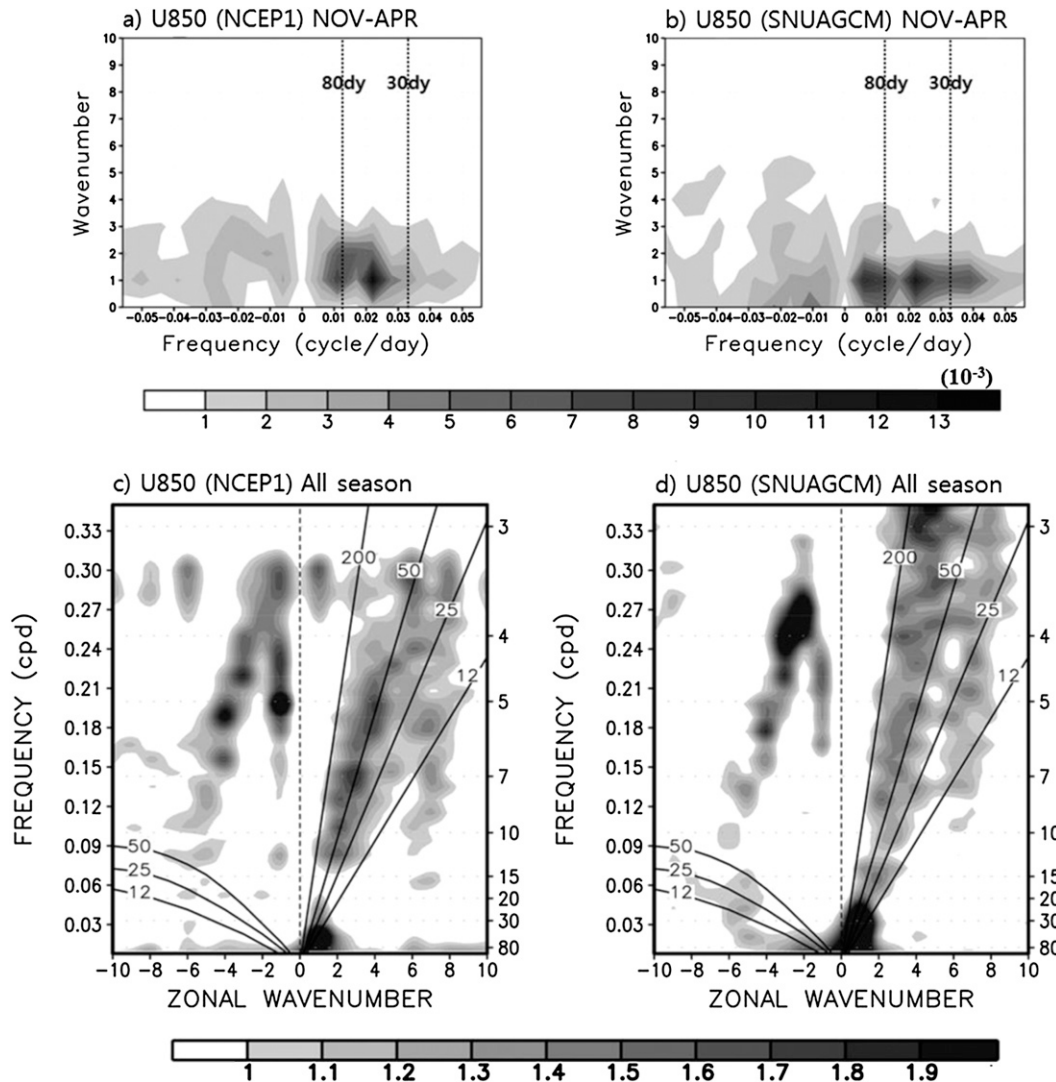


FIG. 1. (top) November–April zonal wavenumber–frequency spectra of 850-hPa zonal wind averaged for 5°N–5°S from (a) NCEP 1 and (b) the SNU AGCM. (bottom) All-season zonal wavenumber–frequency spectra of 850-hPa zonal wind for the 15°N–15°S symmetric component from (c) NCEP and (d) SNU AGCM.

at the equator and 155°E is made with a time filter of 30–60 days and then the covariance maps of various variables (geopotential height, wind, and OLR) with respect to the NIOLR time series are obtained and shown in Fig. 2. This methodology is similar to that of Kiladis et al. (2005), which showed the spatial patterns of the upper- and lower-level streamfunctions associated with the MJO. It is noted that the present study used the geopotential height instead of the streamfunction used by Kiladis et al. In the observations (Figs. 2a,c), the upper- and lower-level wind fields are characterized by upper-level divergence and lower-level convergence over the convection region, and the associated pressure pattern at 200 hPa is characterized by high

and low centers to the east and west of the convection, respectively, and vice versa at 850 hPa. Those geopotential height and wind fields appear to be similar to those associated with the forced Kelvin wave in the tropics (Matsuno 1966), whereas off the equator, the Rossby wave contribution to the wind field appears to be large, particularly in the upper level. Figures 2b and 2d are the GCM counterparts of the observed MJO patterns shown in Figs. 2a and 2c, respectively. The main features of the observed MJO pattern shown above are reasonably well reproduced by the GCM. It is also pointed out that the GCM geopotential height pattern in the subtropical Pacific is somewhat different from the observations, particularly in the lower level. In the GCM, the lower-level geopotential

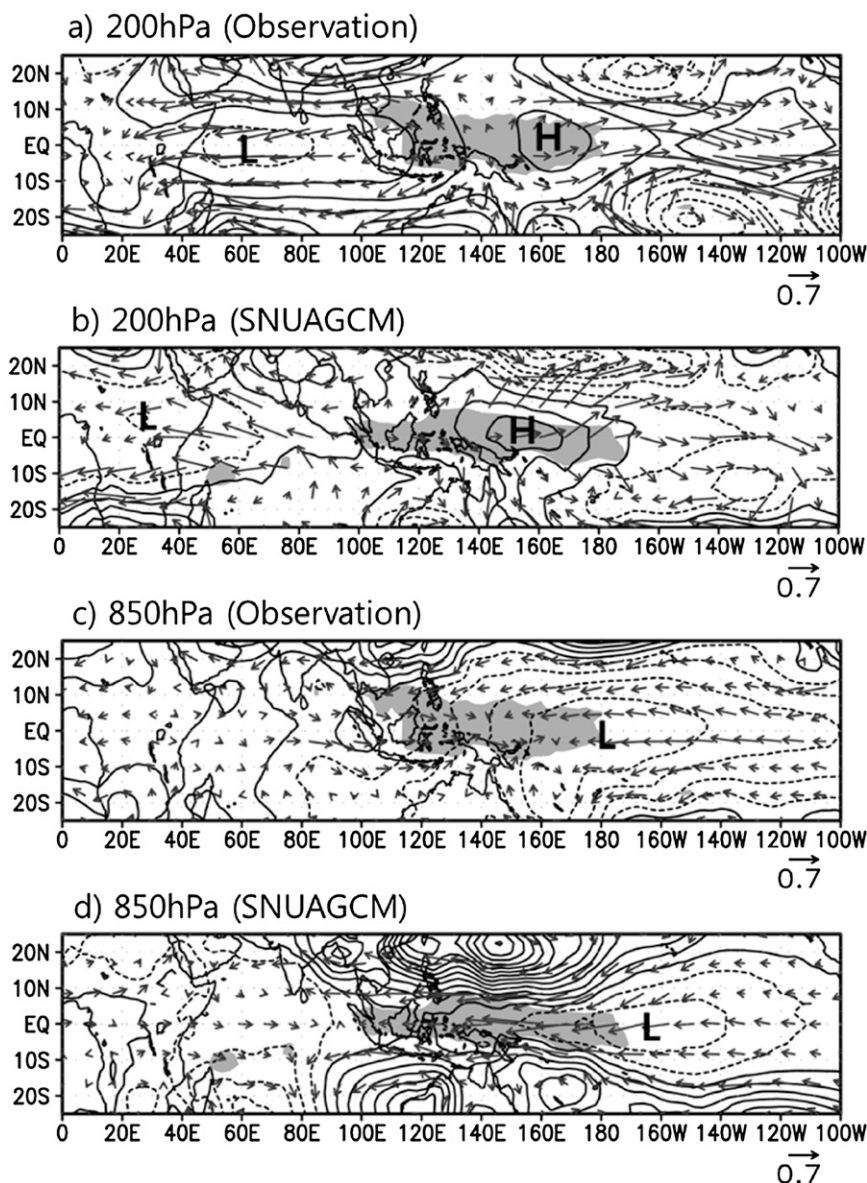


FIG. 2. Regression maps of OLR (shading), geopotential height (contour), and horizontal wind (vector) anomalies associated with OLR variations on the 30–60-day time scale and the wave-number 1–2 component (the base point is the equator and 155°E) for (a),(c) observations [European Centre for Medium-Range Weather Forecasts (ECMWF) Interim Re-Analysis; National Oceanic and Atmospheric Administration (NOAA) OLR] and (b),(d) the SNU AGCM. Shading denotes OLR anomalies $< -3.5 \text{ W m}^{-2} \sigma^{-1}$. Solid (dashed) contours denote the positive (negative) geopotential height anomalies. The contour interval is $0.7 \text{ m } \sigma^{-1}$ at the 850-hPa level and $1.4 \text{ m } \sigma^{-1}$ at the 200-hPa level.

anomalies in the subtropical western Pacific are located more to the south than in the observations. As a result, the equatorial zonal wind (the easterlies) over the convection is more affected by the subtropical high and is less affected by the equatorial Kelvin wave, whereas in the observations the equatorial wind field near the convection appears to be more affected by the forced Kelvin wave. This difference may be related to poor simulation

of monsoon circulation in the western Pacific (Kang et al. 2002).

Although certain differences exist, overall, the GCM is able to reproduce the observed characteristics of the MJO in the tropics reasonably well. In the next section, the aqua-planet experiments are carried out with the GCM with different meridional structures of SST to investigate the impact of SST on the intraseasonal disturbances.

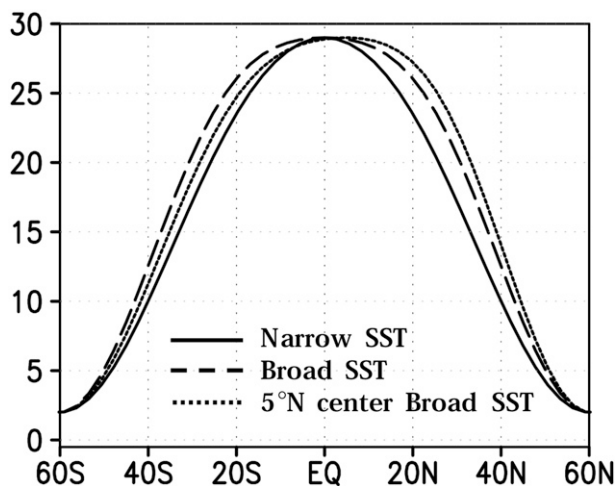


FIG. 3. Zonal-mean aqua-planet simulations for SST ($^{\circ}\text{C}$) that are (solid) narrow, (long dashed) broad, and (short dashed) broad with the center shifted to 5°N .

3. Aqua-planet experiments

The behavior of the general circulation model is often masked by the complexity of the boundary conditions, including zonal asymmetries caused by SST, topography, and land–sea distributions that complicate the interpretation of the model results. These considerations motivated us to use a model with much simpler forcings. One of the idealizations is to run the model under axially symmetric forcings, and this approach has been used in many previous studies, for example, the aqua-planet experiments of Hayashi and Sumi (1986), Randall et al. (1991), Lee et al. (2001, 2003), and Maloney et al. (2010). The aqua-planet experiment can be regarded as an idealized Atmospheric Model Intercomparison Project (AMIP) simulation, in which full physical parameterizations are retained, but the lower boundary conditions of the model are simplified with a fixed, zonally symmetric SST distribution and perpetual solar irradiance at equinox conditions. In this configuration, sensitivity experiments were performed by varying the underlying SST distributions.

The meridional profiles of the zonally uniform SSTs used in the present aqua-planet experiments are shown in Fig. 3. The SST profiles were obtained from Neale and Hoskins (2000), except that 2°C was uniformly added, because the SST of Neale and Hoskins is somewhat cooler than that observed near the equator. For simplicity, the profiles of the solid and long-dashed lines are referred to as “narrow” and “broad” SST, respectively. Figure 4a shows the wavenumber–frequency spectrum of an 850-hPa zonal wind simulated by the aqua-planet GCM with the narrow SST. Clearly, the eastward-propagating wave of wavenumber 1 is the most dominant

mode of the disturbances simulated. The wave speed (with a period of about 20 days) is faster than those of the observed and simulated MJO shown in Fig. 1. This wave spectrum is also presented by the space–time power spectrum of Wheeler and Kiladis (1999). As seen in Fig. 4b, the simulated variances of U850 in the tropics are dominated by contributions from convectively coupled Kelvin waves, whose maximum variances coincide well with the dispersion curves of the Kelvin waves obtained from the shallow water theory (e.g., Matsuno 1966; Wheeler and Kiladis 1999). The equivalent depths of the Kelvin waves are between 12 and 50 m, and the phase speeds of those waves are between 11 and 22 m s^{-1} . These simulated moist Kelvin waves are also seen in the observations (Fig. 1c), although the intensity of the waves is weaker in the observations. In contrast to the observations and the GCM simulation with the realistic boundary conditions, the westward-propagating waves, particularly the Rossby waves, are very weak and invisible. Because the aqua planet does not provide any asymmetric (wave) component of external forcing, the waves simulated in this framework should be generated by atmospheric internal dynamics. The present results indicate that the tropical disturbances are generated mainly by the dynamics associated with the moist Kelvin waves. One of the possible dynamics is the moist unstable Kelvin waves (Wang 1988; Wang and Rui 1990), where the Kelvin waves become unstable by condensational heating with a sufficient moisture supply, whereas the Rossby waves are damped.

The broad SST shown in Fig. 3 was prescribed as a surface boundary condition of the aqua-planet GCM and the model was integrated for 10 years as in the control experiment. Figure 5a shows the counterpart of Fig. 4a. Interestingly, the propagating speed of the dominant wave for the broad SST case, with a period of about 30 days, is slowed down relative to the narrow SST case. In addition, the westward-propagating waves become more visible relative to the narrow SST case. Figure 5a also shows that the eastward-propagating waves become weaker than those of the narrow SST and a strong signal of westward-propagating waves appears in the intra-seasonal time scales (about 100 days) of wavenumber 3. When the SST center is shifted to 5°N (Fig. 5b), the eastward-propagating waves are further slowed down with wave periods of 30–60 days. To see actual wave propagation characteristics, Hovmöller diagrams of 850-hPa zonal wind along the equator are shown in Fig. 6 for the three aqua-planet experiments. An arbitrary 1-yr period is taken among the 10-yr simulation period. In the narrow SST case (Fig. 6a), the eastward propagation appears regularly all along the equatorial circle and the propagation speed is relatively fast (about 20 days). But

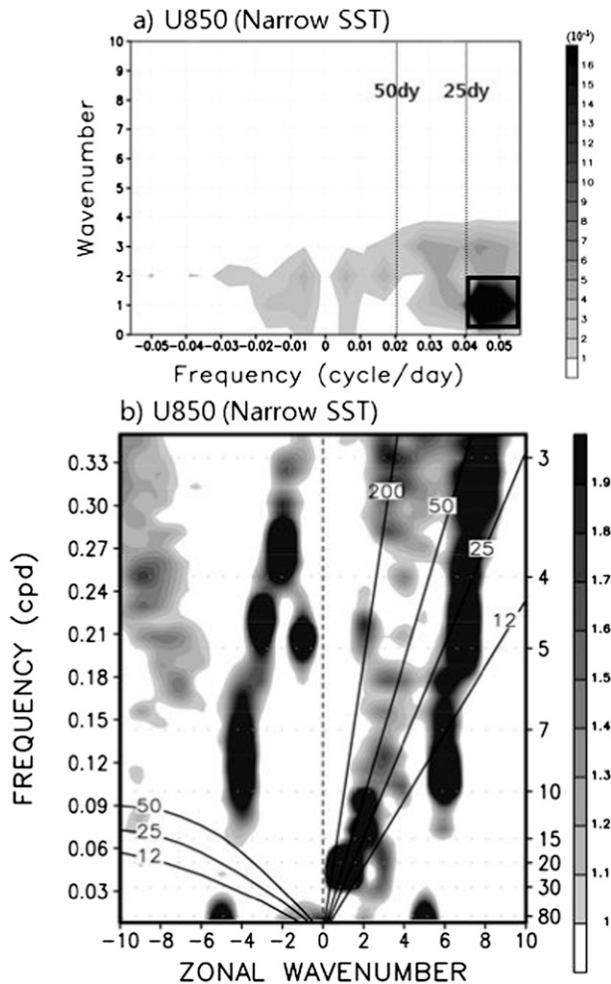


FIG. 4. (a) Zonal wavenumber–frequency spectrum of 5°N–5°S-averaged 850-hPa zonal wind from the aqua-planet SNU AGCM with the narrow SST. The thick box indicates the dominant time scale and zonal wavenumber of the equatorial waves. (b) Zonal wavenumber–frequency spectrum of the 15°N–15°S symmetric component of OLR from the aqua-planet SNU AGCM with the narrow SST.

in the broad SST case (Fig. 6b), the eastward-propagating signals, which are slower than those of the narrow SST, appear spontaneously. In the SST with its center at 5°N (Fig. 6c), the eastward-propagating waves, appearing as spontaneously as in the broad SST case, are even slower than those of the other cases. However, the eastward-propagating signals that cross the equatorial circle are also seen in some periods, as indicated by a long arrow. In Fig. 6c, the westward-propagating signals are also seen in certain periods, as indicated by short arrows in the figure. These westward-propagating waves seem to be related to the unstable Rossby waves when the warm SSTs are located off the equator. The dynamics of unstable Rossby waves in warm SST conditions off the

equator will be discussed in the next section. It is noted that the observed MJO also appears more or less spontaneously in a limited region, mainly over the Indian and western Pacific Oceans. It is also noted that the observations show that the maximum SST is shifted off the equator (few degrees north) along the ITCZ region and is in the western Pacific. The results indicate that the broad SST in the western Pacific and the off-equatorial position of the maximum SST plays an important role in formulating the observed MJO.

Figure 7 shows the spatial patterns of 850-hPa geopotential height, 850-hPa wind, and OLR anomalies associated with the fast Intraseasonal Oscillation (ISO) mode of the narrow SST case (Fig. 7a) and the relatively slow mode of the broad SST case (Fig. 7b). The results were obtained by isolating the anomalies, whose time scales and zonal wavenumbers are limited to those inside of the thick boxes in Fig. 4a (zonal wavenumber: 0.3–2; frequency: 0.04–0.055) and Fig. 5a (zonal wavenumber: 0.3–2; frequency: 0.025–0.04). In practice, these dominant time scale and wavenumber components were filtered from OLR at the equator and 110°E and regressed to all anomaly fields (the horizontal wind, geopotential height at 850 hPa, and OLR).

The fast ISO mode (Fig. 7a) is characterized by the equatorial Kelvin waves, and the Rossby component is not distinctive in the equatorial region. On the other hand, the broad SST (Fig. 7b) produces the Rossby component strongly coupled with the equatorial Kelvin wave even in the equatorial region. As a result, the zonal wind and geopotential height are in a quadrature relationship. The underlying dynamics associated with the slow MJO mode appear to be related to the coupling between Kelvin and Rossby waves, which is excited more in the broad SST and off-equatorial SST cases. The impact of SST on the coupling of the Rossby and Kelvin waves is examined in more detail with a simple model in the next section.

4. Analytical model

Here, we adopted the theoretical model developed by Wang (1988) and Wang and Rui (1990). This is a one-and-a-half-layer model, which includes the first-baroclinic mode of the free troposphere and a barotropic PBL mode. Interactive moisture physics is added in the model with convective heating resulting from the vertical moisture flux in the lower layer. The vertical moisture flux can be induced by the large-scale horizontal moisture convergence in the lower layer and the frictional convergence in the planetary boundary layer. The governing equations are based on the longwave approximation:

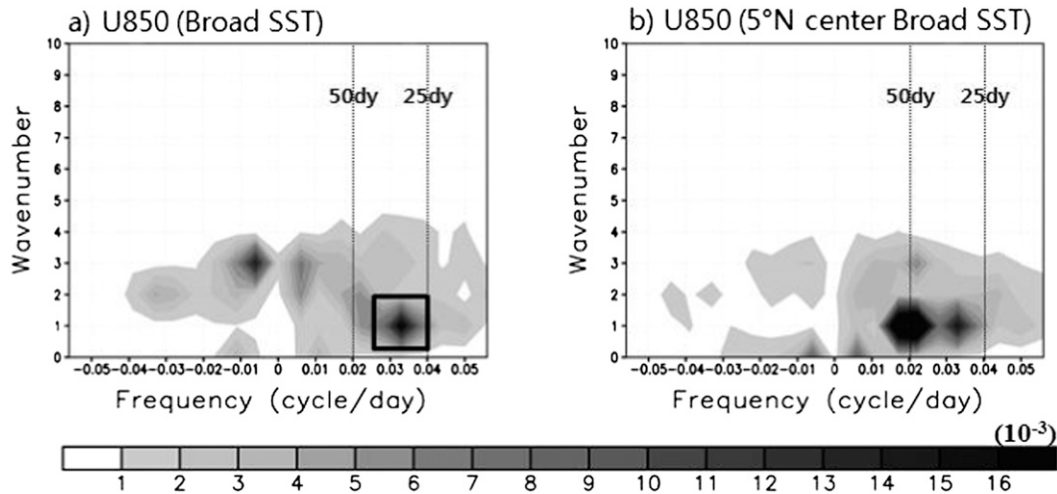


FIG. 5. Zonal wavenumber–frequency spectra of 5°N–5°S-averaged 850-hPa zonal wind from the aqua-planet SNU AGCM with the (a) broad SST and (b) broad SST with its center shifted to 5°N. The thick box indicates the dominant time scale and zonal wavenumber of the equatorial waves.

$$\begin{aligned}
 u_t - \beta y v + \phi_x &= -\kappa \nabla^2 u, & (1) \quad & \text{where } u, v, \text{ and } \phi \text{ are the zonal and meridional winds and the geopotential height. Here, } \beta = 2.3 \times 10^{-11} \text{ m}^{-1} \text{ s}^{-1} \\
 \beta y u + \phi_y &= 0, \quad \text{and} & (2) \quad & \text{is the meridional variation of the Coriolis parameter and } y \text{ is the latitude. Note, } \kappa \text{ is a coefficient of diffusion and } N \\
 \phi_t + C_0^2(u_x + v_y) &= Q - N\phi, & (3) \quad & \text{is a coefficient related to Newtonian cooling. The variable}
 \end{aligned}$$

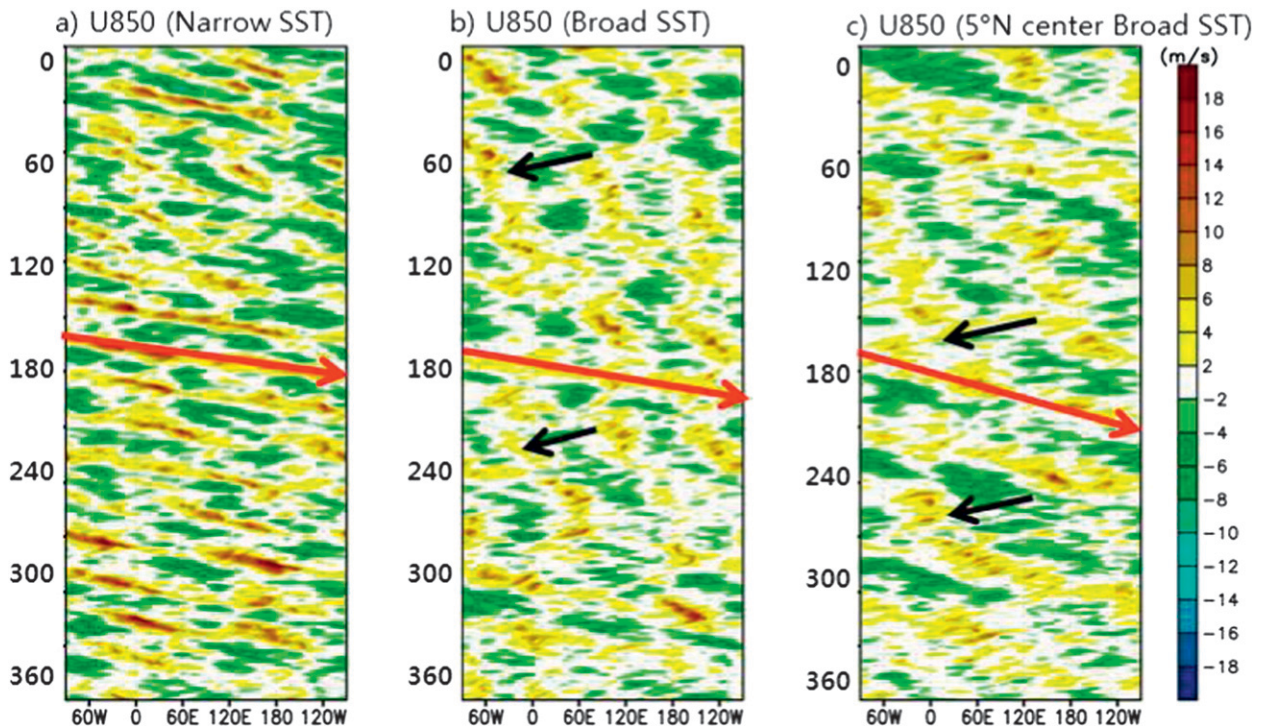


FIG. 6. Longitude–time cross sections of the 850-hPa zonal wind simulated by aqua-planet GCM with (a) narrow SST, (b) broad SST, and (c) broad SST with its center shifted to 5°N. The 850-hPa zonal wind is meridionally averaged between 5°S and 5°N. The time period of 1 yr is arbitrarily chosen from the equilibrium state in each model. Red arrow indicates eastward-propagating wave. Black arrows indicate westward-propagating wave.

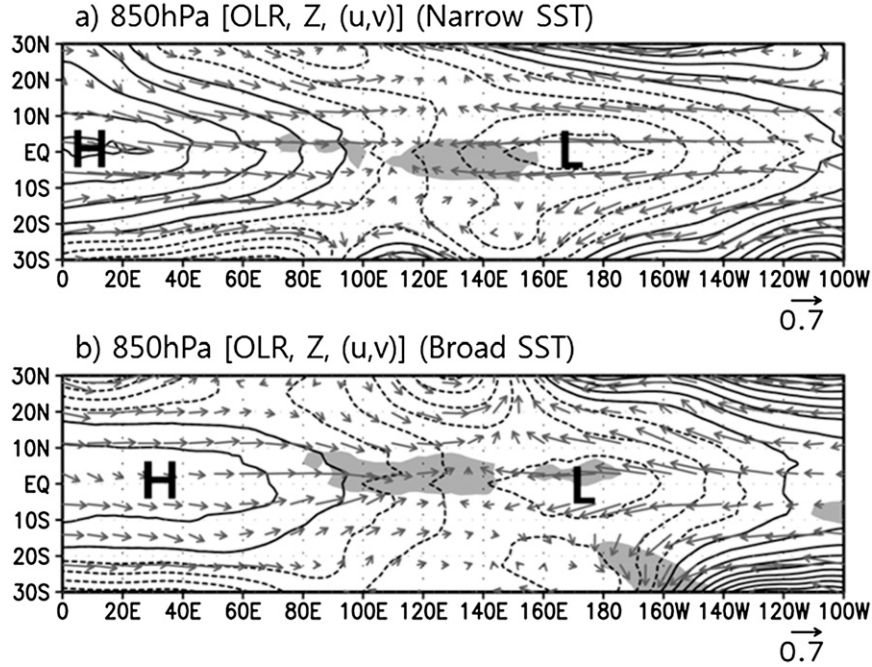


FIG. 7. Regression maps of OLR (shading), 850-hPa geopotential height (contour), and 850-hPa wind (vector) anomalies associated with OLR variations on the dominant time scale and wavenumber component (the base point is the equator and 110°E) from the aqua-planet SNU AGCM with the (a) narrow and (b) broad SST. The shading denotes the OLR anomalies less than $-3.5 \text{ W m}^{-2} \sigma^{-1}$. The solid (dashed) contours denote the 850-hPa positive (negative) geopotential height anomaly. The contour interval is $0.7 \text{ m } \sigma^{-1}$.

C_0 is the gravest internal gravity wave speed. The latent heating term Q can be written as (Wang 1988)

$$Q = bL/\Delta p \times \left\{ -1/g \int_{p_M}^{p_B} \nabla \cdot [q(p)\mathbf{V}] dp + [(q_B - q_L)/g] bW_b \right\}, \quad (4)$$

here L denotes the latent heat of condensation, g is gravity, $b = 0.6$ is the fractional moisture converted into rainfall, $\Delta p = 400 \text{ hPa}$ is the half pressure depth of the free atmosphere, \mathbf{V} is horizontal wind, q_B and q_L represent the mean specific humidity at the boundary layer and the lower free atmosphere (respectively), and $p_B = 900 \text{ hPa}$ and $p_M = 500 \text{ hPa}$ are the pressure at the top of the PBL and middle troposphere (respectively). The first term of Eq. (4) represents the free tropospheric moisture convergence and the second term represents the moisture convergence caused by boundary layer Ekman pumping W_b . In the present model, the first term can be approximated by $q_c(\mathbf{V} \cdot \nabla)$, where q_c is the mean specific humidity at the lower layer, which is defined later.

A unique feature of this model is the control of SST on an atmospheric basic-state moisture field and the

associated static stability, which is critical for MJO dynamics. As in Wang (1988), the moisture profile is assumed to decrease upward exponentially from q_s at the surface with an e -folding scale of 2.2 km , that is, $q(p) = q_s(p/p_s)^{7.6/2.2-1}$, and the surface specific humidity is assumed to be the sole function of SST, $q_s = (0.972 \times \text{SST} - 8.92) \times 10^{-3}$. Thus, the three-dimensional distribution of basic-state moisture and static stability are functions of SST.

At the top of the PBL, W_b can be derived from the steady boundary layer momentum equation for low-frequency motion (Wang and Li 1994):

$$-\beta y v_b = -\phi_{bx} - \varepsilon u_b \quad \text{and}$$

$$\beta y u_b = -\phi_{by} - \varepsilon v_b,$$

where ϕ_b , u_b , and v_b denote the geopotential height and the zonal and meridional winds in the barotropic boundary layer, and ε is a damping coefficient with a time scale of 0.5 days. As in Wang and Li (1994), the geopotential height perturbation at the PBL was assumed to be equal to the lower free atmosphere and a semigeostrophic PBL was used here, where the disturbances have a larger zonal than meridional scale. The

Ekman pumping velocity (i.e., W_b) can be obtained as $W_b = -\Delta p_b(d_1\phi_{yy} + d_2\phi_y)$, where $\Delta p_b = 100$ hPa is the PBL pressure depth, $d_1 = \varepsilon/(\varepsilon^2 + \beta^2 y^2)$, and $d_2 = -2\varepsilon\beta^2 y/(\varepsilon^2 + \beta^2 y^2)^2$.

After considering the heating term of Eq. (4), Eqs. (1)–(3) can be nondimensionalized by using a characteristic velocity $C_0 = \sqrt{S/(\Delta p/2)^2} \approx 50 \text{ m s}^{-1}$ [the gravest internal gravity wave speed; Wang (1988)] and length scale $L = \sqrt{C_0/\beta} \approx 1460 \text{ km}$, and time scale $T = 1/\sqrt{\beta C_0} \approx 0.34$ day. Then, the governing equations of the present simple model become the following:

$$u_t - yv + \phi_x = -\kappa \nabla^2 u, \quad (5)$$

$$yu + \phi_y = 0, \quad \text{and} \quad (6)$$

$$\phi_t + (u_x + v_y) = (\text{SST} - 9.2)[\alpha(u_x + v_y) - \gamma(d_1\phi_{yy} + d_2\phi_y)] - N\phi, \quad (7)$$

where $\alpha = (b\Delta p/p_M)q_c(LR/C_0^2 C_p)$, $\gamma = (1/\varepsilon)(b\Delta p_b/p_M)(q_b - q_c)(LR/C_0^2 C_p)$, R is the gas constant, $q_c = (1/\Delta p) \int_{p_M}^{p_b} q(p) dp$, and $q_b = (1/\Delta p_b) \int_{p_b}^{p_s} q(p) dp$. The surface pressure $p_s = 1000$ hPa, the PBL depth $\Delta p_b = 100$ hPa, $d_1 = \varepsilon/(\varepsilon^2 + y^2)$, and $d_2 = -2\varepsilon y/(\varepsilon^2 + y^2)^2$. Note that q_b and q_c are functions of SST as we used a given vertical profile of specific humidity and the saturated specific humidity at the surface is a function of SST. Typical values of α and γ are 0.045 and 0.04, respectively.

Assuming that the SST has the following meridional structure:

$$\text{SST} = \text{SST}_0 \exp\{-(y - y_0)/y_L\}^2\}, \quad (8)$$

where $\text{SST}_0 = 29.5^\circ\text{C}$, y_0 is the SST center latitude, and y_L is the meridional e -folding scale of the SST. Equations (5)–(8) compose a set of linear partial differential equations, for which the eigenvalue problem can be readily solved. For the zonal-propagating plane waves, the general solution has a structure of $e^{i(kx - \sigma t)}$, where k is the zonal wavenumber and σ is the frequency. The phase speed and growth rate are defined by $\text{Re}(\sigma)/k$ and $\text{Im}(\sigma)$, respectively. Different from Wang and Rui (1990), for simplicity, only the lowest three meridional modes of each variable are kept for the meridional expansion of the parabolic cylinder functions, which capture the fundamental characteristics of the lowest Rossby and Kelvin waves. Another new feature is that we define a parameter that measures the relative contribution of Kelvin and Rossby waves to the model's MJO mode. Because the equatorial Kelvin wave has equatorial, but the Rossby wave has off-equatorial precipitation, we use the ratio of the precipitation magnitude between the off-equatorial (15° – 25°N) and equatorial

(5°S – 5°N) regions to represent the relative ratio between Rossby and Kelvin components (R/K ratio).

First, the SST center is specified at the equator (i.e., $y_0 = 0$) and the meridional SST scale (i.e., y_L) is changed to study how SST changes modify the coupling of Rossby and Kelvin waves. Figure 8a clearly shows that this model selects the long waves to become unstable and the most unstable wave has a wavenumber 1. The selection of long waves for instability is partly because of the large surface friction and strong momentum diffusion of short waves in the free atmosphere, indicating the importance of a damping mechanism for tropical intraseasonal fluctuations. When SST is strongly trapped near the equator (i.e., $y_L = 10^\circ$), this model presents fast eastward modes, which have a phase speed of 20 m s^{-1} for wavenumber 1, and shorter waves propagate eastward even faster. Figure 8b shows that for the narrow SST (i.e., $y_L = 10^\circ$), the R/K ratio is very small and the model presents a strong eastward-propagating Kelvin-type mode, whose spatial pattern is shown in Fig. 9a. When the SST becomes broader, this model presents a stronger Rossby component (Figs. 8b, 7b); meanwhile, the phase speeds also decrease to the range of the MJO, about 5 m s^{-1} . It is noted that the present analytic model is based on a linearized shallow water equation in an equatorial beta plain, and therefore the equatorially trapped waves are emphasized and off-equatorial waves are not well captured in the model. In spite of its simplicity, the model produces the most unstable modes, whose spatial patterns (shown in Fig. 9) are similar to the counterparts of the aqua-planet GCM shown in Fig. 7, particularly in the tropics. The results of the simple model explain the GCM solutions (Figs. 4, 5) that only the narrow SST prefers to enhance the fast eastward Kelvin waves, while the broad SST provides enough off-equatorial moisture for the growth of the Rossby component, which couples with the Kelvin component strongly and slows down the eastward modes.

One factor influencing the phase speed of the unstable mode is the gross moist stability M , which can be expressed as $M = 1 - \alpha(\text{SST} - 9.2)$ in Eq. (7). The values of the broad and narrow SSTs averaged over the tropics between 20°S and 20°N are 27.5° and 17.5°C , respectively, and accordingly, 0.13 and 0.6 for the M values. Therefore, the phase speeds of the broad and narrow SSTs are 36% and 77% of the dry Kelvin wave speed of 50 m s^{-1} . This is simply because of more moisture availability in the broad SST case and more moisture convergence near the equator. This lower-level moisture convergence is not sufficient to generate the MJO slow mode.

Another important mechanism, which affects the phase speed and instability, is the PBL frictional convergence

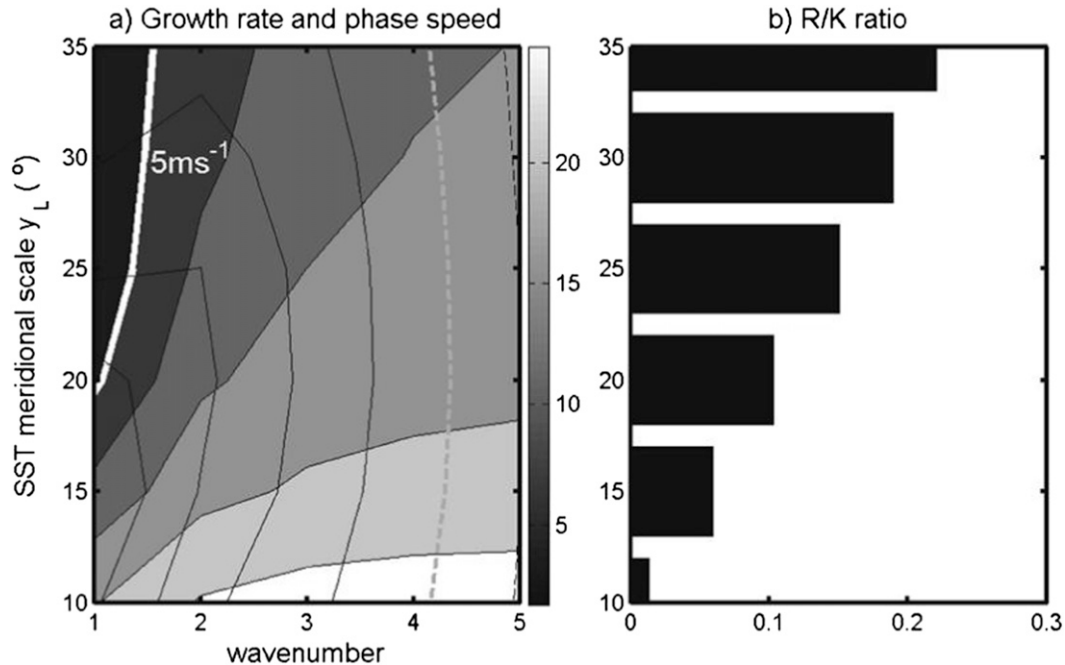


FIG. 8. (a) Growth rate (contour) and phase speed (shading) as functions of the wavenumber and meridional SST scale (i.e., y_L). Positive (negative) contours are solid (dashed) and zero contours are indicated by gray dashed lines. The contour interval is 0.2 times the magnitude of 0.2 day^{-1} . (b) R/K component as functions of the meridional SST scale where $y_0 = 0$.

(Wang 1988). Because the Kelvin component contributes the major part of the convectively coupled Kelvin–Rossby waves in the present model, as shown in Figs. 8b and 9b, we focus on the Kelvin component in the following discussion. Considering only the Kelvin component, near the equator, $d_1 \approx 1/\varepsilon$ and $d_2 \approx 0$, and Eqs. (5)–(7) without the diffusion term can be combined as $\phi_{tt} - B\phi_t - M\phi_{xx} = 0$, where $B = 2\gamma(\text{SST} - 9.2)/\varepsilon$. The small term with the order of $O(y^2)$ has been omitted near the equator. For the wave solutions, the frequency is $\sigma = iB/2 + \sqrt{Mk^2 - B^2/4}$ and the zonal phase speed is $\text{Re}(\sigma)/k = \sqrt{M - B^2/4k}$. Therefore, the phase speed can be slowed down by the PBL frictional convergence and the slowdown is more significant for longer waves (smaller k). As noted before, the frictional convergence term affects the Kelvin wave instability. The equation of σ can have an imaginary value ($iB/2$) by adding the terms associated with the frictional moisture convergence, meaning that the PBL frictional terms add the instability of the planetary-scale Kelvin waves. This additional instability is wavelength independent. However, the frictional diffusion ($-\kappa \nabla^2 u$) will dampen short waves strongly and select the longest wave to become the most unstable (Fig. 8a).

Next, we examined the role of the SST center on the coupled Kelvin–Rossby waves. In the boreal summertime, the ITCZ shifts northward, and the lower-tropospheric

southerly winds produce strong moisture accumulation off the equator of the NH. Such an ITCZ shift is associated with a shift of the SST center off the equator to the NH. The off-equatorial SST center can be represented by $y_0 > 0$ in Eq. (8). When the SST is centered at the equator, this model presents strong unstable eastward but damped westward modes (Fig. 10). With the broad SST the slow eastward mode has a considerable Rossby component, although it is still smaller than the eastward Kelvin component (Fig. 8b). When the SST center moves poleward, the eastward modes become less unstable and eventually are damped as seen in Fig. 10. This is because equatorial moisture is too small to support the growth of the Kelvin component. On the contrary, the westward modes obtain enough off-equatorial moisture for the Rossby component, and even become unstable when the SST center is located further north of 15°N . To check the validity of the simple model solution for the SST whose center is way off the equator (the model is on an equatorial beta plane), we have made an aqua-planet simulation with the SST whose center is located at 20°N . The simulation clearly shows the westward-propagating convection signals along the equator, but the westward-moving disturbances have two distinctive time scales of about 2 weeks and about 2 months (not shown). The disturbance whose time scale is 2 weeks appears to be related to a single

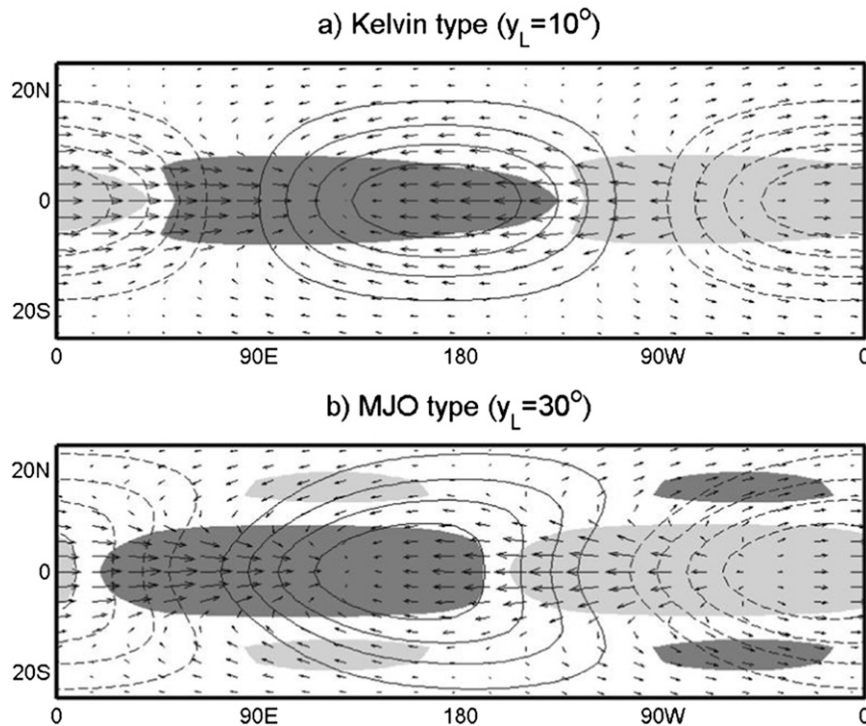


FIG. 9. Horizontal structures of wavenumber 1 with the meridional SST scale of (a) $y_L = 10^\circ$ and (b) $y_L = 30^\circ$, respectively. Temperature (contours), precipitation (shading), and wind vectors are shown. Positive (negative) shades are dark gray (light gray) and only precipitation above one-third of the magnitude is shaded. Positive (negative) contours are solid (dashed). The contour interval is one-fifth of the magnitude and zero contours are not drawn. Here, $y_0 = 0$.

convection resulting from the unstable Rossby mode shown in Fig. 10, and the slow-propagating mode seems to be associated with convective clusters, which cannot be explained with the present simple model. It is pointed out that these solutions are based on the meridional SST profile given by Eq. (8). In reality, during a boreal summer, the SST at the equator is still very warm, though slightly cooler than the off-equatorial SST. In such a situation as seen in Figs. 8 and 10, the SST's broadening effect in addition to the center shift affects the phase speed of the coupled waves significantly, and therefore, the eastward phase speed is much slowed down and the westward waves are excited. When the SST is centered at 10°N , an off-equatorial rainband associated with the eastward modes (Fig. 11a) appears to be similar to the summer rainband of the intraseasonal oscillation during the boreal summer in India and the western Pacific region (Wang and Xie 1997). For SSTs located further poleward, this simple model presents unstable westward Rossby-type disturbances (Fig. 11b). Without the role of the vertical-mean shear, this model only presents the weakly unstable Rossby modes presented by Xie and Wang (1996).

5. Summary and concluding remarks

In the present study, the dynamics of the Madden-Julian oscillation simulated by the aqua-planet GCM are investigated using the simple theoretical model of Wang and Rui (1990), which is a one-and-a-half-layer model with a first-baroclinic mode and a planetary boundary layer. The aqua-planet GCM experiments used a full atmospheric GCM, but the SST was prescribed with the zonally symmetric one. When realistic surface boundary conditions (observed SST and land configuration) were prescribed, the GCM used here reproduced the observed characteristics of the MJO reasonably well. The aqua-planet GCM prescribed with a zonally symmetric SST, whose meridional structure is relatively narrow, simulates strong intraseasonal and eastward-propagating disturbances in the tropics. However, the phase speed of the eastward propagation is much faster (a period of about 20 days) than that of the MJO simulated by the full GCM, indicating that the surface boundary conditions including the SST are important factors for formation of the MJO. A series of aqua-planet experiments with different meridional structures of the SST showed that

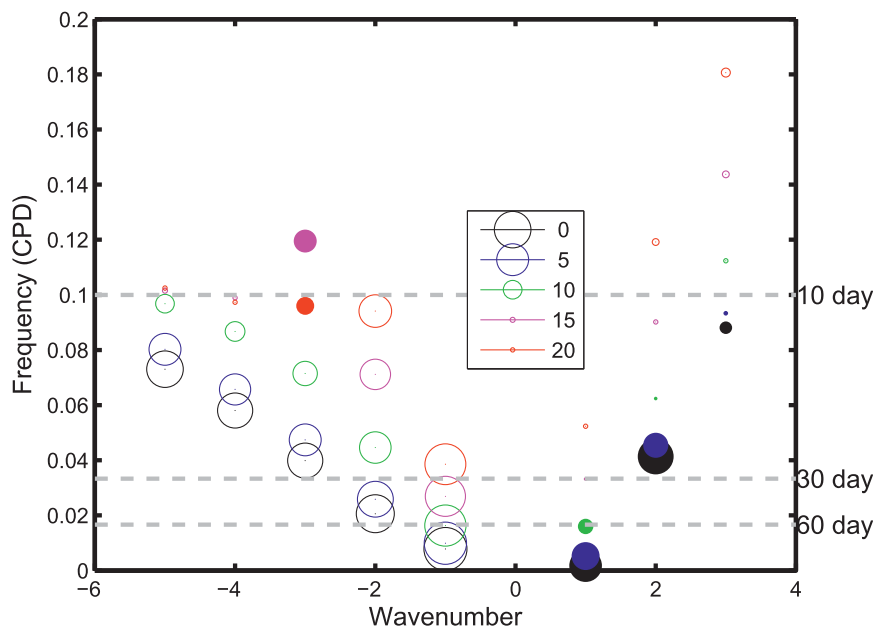


FIG. 10. Frequency and growth rate as a function of the wavenumber. Unstable and damped modes are represented by dots and circles, respectively. The growth rates are proportional to the diameters, with respect to the maximum growth and damping rate of 0.13 and -0.6 day^{-1} , respectively. Results with different SST centers are denoted by different colors in the legend. Here, $y_L = 25^\circ$.

indeed the broader SST (less meridional gradient of the SST) in the tropics slows down the phase speed and weakens the fast unstable Kelvin waves but excites the westward-propagating Rossby waves more. The results are interpreted such that the SST structure determines the horizontal structure of the coupled Kelvin–Rossby waves in the tropics (Wang and Rui 1990) and the ratio between the Kelvin and Rossby wave amplitudes determines the phase speed and amplitude of the MJO. Stronger Rossby waves with the broader SST result in the slowing down of the eastward-propagating coupled waves.

The impact of SST on the coupled Kelvin–Rossby waves is also investigated using the model of Wang and Rui (1990). As seen in the aqua-planet experiments, the propagation speed and amplitude of the coupled waves depend on the structure of the SST, which directly affects the lower-level moisture field in the present model. The spatial mean of the tropical SST, which is different for different meridional structures of the SST, affects wave instability by influencing the moist static stability and the latent heating in the free atmosphere by the frictional moisture convergence near the surface. The longer waves are more unstable. The narrow SST prefers to enhance only the fast eastward Kelvin waves, while the broad SST provides enough off-equatorial moisture for the growth of the Rossby component, coupled with

the Kelvin component, and slows down the eastward modes. It is also shown that when the SST center moves poleward, the eastward modes become less unstable and eventually are damped because the equatorial moisture is too small to support the growth of the Kelvin component. On the contrary, the westward modes obtain enough off-equatorial moisture for the Rossby component, and even become unstable when the SST center is located further north of 15°N . The phase speed of the eastward modes became faster when the SST center shifted poleward because of less moisture (associated with the cooler SST near the equator) supplied to the equatorial Kelvin wave. When the SST moves further poleward, this model presents unstable westward Rossby-type disturbances.

It is pointed out that the dynamics and physics of both aqua-planet and full GCM are the same. The only difference between the aqua-planet and the full GCM are the boundary conditions. Although the same dynamics are operating in both the aqua-planet and full GCMs, the normal modes appearing in the models depend on the boundary conditions. The point here is that the degree of coupling between the Kelvin and Rossby waves (contribution of the Rossby waves in the coupled Kelvin–Rossby waves) depends on the SST boundary conditions. The present results can be applied to understanding the observed MJO. In the observations, the

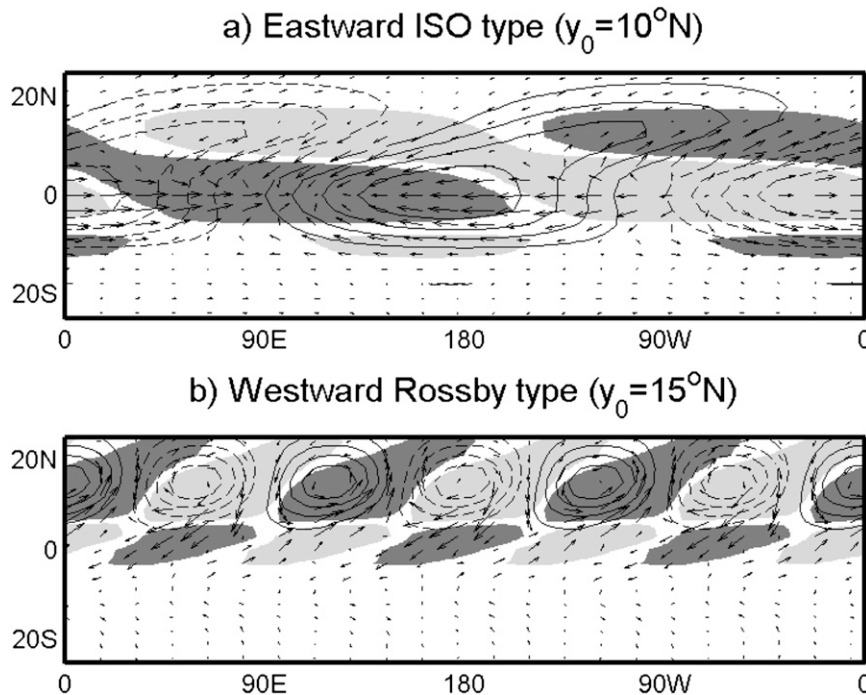


FIG. 11. As in Fig. 9, but for the (a) eastward intraseasonal oscillation-type and (b) westward Rossby-type modes with the SST centered at 10° and 15°N , respectively. Wavenumbers 1 and 3 are drawn for the unstable eastward and westward modes, respectively. Here, $y_L = 25^\circ$.

surface boundary conditions have a complicated spatial structure with land, ocean, and mountains. All of those are matters for determining the detailed structure of the MJO. In simplicity, the broader SST structure in the present study can be a counterpart of the tropical warm pool over the Indian Ocean and western Pacific, where the MJO has a strong eastward-propagation component with a slow time scale, but the MJO speed becomes faster in the eastern Pacific, whose SST structure is similar to that of the narrower SST. It is expected that the monsoon resulting from land-sea contrast also strongly influences the MJO particularly during boreal summer, when the mean precipitation and large moisture are shifted to the subtropical western Pacific and continental side. The effects of monsoons, a warm pool, and the cold tongue of the tropical SST on the MJO could be the topic for a future study.

Overall, the meridional structure of the moisture source, determined by the SST structure, plays a critical role in determining the characteristics of convectively coupled Kelvin-Rossby waves and in formulating the MJO. It is mentioned that in the present study, the convection (precipitation) is assumed to be determined by a steady-state balance between precipitation and moisture convergence. However, by adding the tendency term of the moisture equation, the existence of the moisture mode was demonstrated by Majda and Stechmann

(2009) and Sobel and Maloney (2012). In their studies, however, the governing equations of the circulation system, determining the moisture convergence, were crudely treated. It may be interesting to examine how the results of the present study can be modified by considering a comprehensive moisture equation combined with a present circulation system. This subject will be a topic of future study.

Acknowledgments. In-Sik Kang was supported by the National Research Foundation of Korea (Grant NRF-2009-C1AAA001-2009-0093042), funded by the Korean Ministry of Education, Science, and Technology (MEST). This work was also supported by the Brain Korea 21 Project.

REFERENCES

- Bechtold, P., M. Koehler, T. Jung, F. Doblas-Reyes, M. Leutbecher, M. J. Rodwell, F. Vitart, and G. Balsamo, 2008: Advances in simulating atmospheric variability with the ECMWF model: From synoptic to decadal time-scales. *Quart. J. Roy. Meteor. Soc.*, **134**, 1337–1351.
- Benedict, J. J., and D. A. Randall, 2009: Structure of the Madden-Julian oscillation in the superparameterized CAM. *J. Atmos. Sci.*, **66**, 3277–3296.
- Chikira, M., and M. Sugiyama, 2010: A cumulus parameterization with state-dependent entrainment rate. Part I: Description and sensitivity to temperature and humidity profiles. *J. Atmos. Sci.*, **67**, 2171–2193.

- Emanuel, K. A., 1987: An air–sea interaction model of intraseasonal oscillations in the tropics. *J. Atmos. Sci.*, **44**, 2324–2340.
- Flatau, M., P. J. Flatau, P. Phoebus, and P. P. Niiler, 1997: The feedback between equatorial convection and local radiative and evaporative processes: The implications for intraseasonal oscillations. *J. Atmos. Sci.*, **54**, 2373–2386.
- Frierson, D. M. W., D. Kim, I.-S. Kang, M.-I. Lee, and J.-L. Lin, 2011: Structure of AGCM-simulated convectively coupled Kelvin waves and sensitivity to convective parameterization. *J. Atmos. Sci.*, **68**, 26–45.
- Fuchs, Z., and D. J. Raymond, 2002: Large-scale modes of a non-rotating atmosphere with water vapor and cloud-radiation feedbacks. *J. Atmos. Sci.*, **59**, 1669–1679.
- Hayashi, Y.-Y., and A. Sumi, 1986: The 30–40 day oscillations simulated in an “aqua-planet” model. *J. Meteor. Soc. Japan*, **64**, 451–466.
- Hendon, H. H., 1988: A simple model of the 40–50 day oscillation. *J. Atmos. Sci.*, **45**, 569–584.
- , 2000: Impact of air–sea coupling on the Madden–Julian oscillation in a general circulation model. *J. Atmos. Sci.*, **57**, 3939–3952.
- , and M. L. Salby, 1994: The life cycle of the Madden–Julian oscillation. *J. Atmos. Sci.*, **51**, 2225–2237.
- Hu, Q., and D. A. Randall, 1994: Low-frequency oscillations in radiative–convective systems. *J. Atmos. Sci.*, **51**, 1089–1099.
- Kang, I.-S., and Coauthors, 2002: Intercomparison of the climatological variations of Asian summer monsoon precipitation simulated by 10 GCMs. *Climate Dyn.*, **19**, 383–395.
- Khouider, B., A. St-Cyr, A. Majda, and J. Tribbia, 2011: The MJO and convectively coupled waves in a coarse-resolution GCM with a simple multicloud parametrization. *J. Atmos. Sci.*, **68**, 240–264.
- Kiladis, G. N., K. H. Straub, and P. T. Haertel, 2005: Zonal and vertical structure of the Madden–Julian oscillation. *J. Atmos. Sci.*, **62**, 2790–2809.
- Kim, D., and I.-S. Kang, 2012: A bulk mass flux convection scheme for climate model: Description and moisture sensitivity. *Climate Dyn.*, **38**, 411–429.
- , and Coauthors, 2009: Application of MJO simulation diagnostics to climate models. *J. Climate*, **22**, 6413–6427.
- , A. H. Sobel, and I.-S. Kang, 2011: A mechanism denial study on the Madden–Julian oscillation. *J. Adv. Model. Earth Syst.*, **3**, M12007, doi:10.1029/2011MS000081.
- Lau, K. M., and L. Peng, 1987: Origin of low-frequency (intraseasonal) oscillations in the tropical atmosphere. Part I: Basic theory. *J. Atmos. Sci.*, **44**, 950–972.
- Lee, M.-I., I.-S. Kang, J.-K. Kim, and B. E. Mapes, 2001: Influence of cloud-radiation interaction on simulating tropical intraseasonal oscillation with an atmospheric general circulation model. *J. Geophys. Res.*, **106** (D13), 14 219–14 233.
- , —, and B. E. Mapes, 2003: Impacts of cumulus convection parameterization on aqua-planet AGCM simulations of tropical intraseasonal variability. *J. Meteor. Soc. Japan*, **81**, 963–992.
- , M. J. Suarez, I. S. Kang, I. M. Held, and D. Kim, 2008: A moist benchmark calculation for atmospheric general circulation models. *J. Climate*, **21**, 4934–4954.
- Lin, J.-L., and Coauthors, 2006: Tropical intraseasonal variability in 14 IPCC AR4 climate models. Part I: Convective signals. *J. Climate*, **19**, 2665–2690.
- Liu, F., and B. Wang, 2012: A model for the interaction between 2-day waves and moist Kelvin waves. *J. Atmos. Sci.*, **69**, 611–625.
- , and —, 2013: Impacts of upscale heat and momentum transfer by moist Kelvin waves on the Madden–Julian oscillation: A theoretical model study. *Climate Dyn.*, **38**, 213–224.
- , G. Huang, and L. Feng, 2012: Critical roles of convective momentum transfer in sustaining the multi-scale Madden–Julian oscillation. *Theor. Appl. Climatol.*, **108**, 471–477.
- Madden, R. A., and P. R. Julian, 1971: Detection of a 40–50 day oscillation in the zonal wind in the tropical Pacific. *J. Atmos. Sci.*, **28**, 702–708.
- , and —, 1972: Description of global-scale circulation cells in the tropics with a 40–50 day period. *J. Atmos. Sci.*, **29**, 1109–1123.
- Majda, A. J., and S. N. Stechmann, 2009: A simple dynamical model with features of convective momentum transport. *J. Atmos. Sci.*, **66**, 373–392.
- Maloney, E. D., 2009: The moist static energy budget of a composite tropical intraseasonal oscillation in a climate model. *J. Climate*, **22**, 711–729.
- , and D. L. Hartmann, 1998: Frictional moisture convergence in a composite life cycle of the Madden–Julian oscillation. *J. Climate*, **11**, 2387–2403.
- , A. H. Sobel, and W. M. Hannah, 2010: Intraseasonal variability in an aquaplanet general circulation model. *J. Adv. Model. Earth Syst.*, **2**, doi:10.3894/JAMES.2010.2.5.
- Matsuno, T., 1966: Quasi-geostrophic motions in the equatorial area. *J. Meteor. Soc. Japan*, **44**, 25–43.
- Matthews, A. J., 2000: Propagation mechanisms for the Madden–Julian oscillation. *Quart. J. Roy. Meteor. Soc.*, **126**, 2637–2651.
- Miura, H., M. Satoh, T. Nasuno, A. T. Noda, and K. Oouchi, 2007: A Madden–Julian oscillation event realistically simulated by a global cloud-resolving model. *Science*, **318**, 1763–1765.
- Moorthi, S., and M. J. Suarez, 1992: Relaxed Arakawa–Schubert: A parameterization of moist convection for general circulation models. *Mon. Wea. Rev.*, **120**, 978–1002.
- Neale, R. B., and B. J. Hoskins, 2000: A standard test for AGCMs including their physical parametrizations. I: The proposal. *Atmos. Sci. Lett.*, **1**, 101–107.
- Neelin, J. D., I. M. Held, and K. H. Cook, 1987: Evaporation–wind feedback and low-frequency variability in the tropical atmosphere. *J. Atmos. Sci.*, **44**, 2341–2348.
- Randall, D. A., Harshvardhan, and D. A. Dazlich, 1991: Diurnal variability of the hydrological cycle in a general circulation model. *J. Atmos. Sci.*, **48**, 40–62.
- Slingo, J. M., and Coauthors, 1996: Intraseasonal oscillations in 15 atmospheric general circulation models: Results from an AMIP diagnostic subproject. *Climate Dyn.*, **12**, 325–357.
- Sobel, A. H., and H. Gildor, 2003: A simple time-dependent model of SST hot spots. *J. Climate*, **16**, 3978–3992.
- , and E. D. Maloney, 2012: An idealized semi-empirical framework for modeling the Madden–Julian oscillation. *J. Atmos. Sci.*, **69**, 1691–1705.
- Sperber, K. R., J. M. Slingo, P. M. Inness, and W. K. M. Lau, 1997: On the maintenance and initiation of the intraseasonal oscillation in the NCEP/NCAR reanalysis and in the GLA and UKMO AMIP simulations. *Climate Dyn.*, **13**, 769–795.
- Stephens, G. L., and J. Haynes, 2007: Near global observations of the warm rain coalescence process. *Geophys. Res. Lett.*, **34**, L20805, doi:10.1029/2007GL030259.
- Tokioka, T., and Coauthors, 1988: The equatorial 30–60 day oscillation and the Arakawa–Schubert penetrative cumulus parameterization. *J. Meteor. Soc. Japan*, **66**, 883–901.
- Waliser, D. E., 1996: Formation and limiting mechanisms for very high sea surface temperature: Linking the dynamics and the thermodynamics. *J. Climate*, **9**, 161–188.

- , 2006: Intraseasonal variability. *The Asian Monsoon*, B. Wang, Ed., Springer, 203–258.
- , K. M. Lau, and J.-H. Kim, 1999: The influence of coupled sea surface temperatures on the Madden–Julian oscillation: A model perturbation experiment. *J. Atmos. Sci.*, **56**, 333–358.
- , S. Schubert, A. Kumar, K. Weickmann, and R. Dole, 2003: Proceedings from a workshop on “modeling, simulation and forecasting of subseasonal variability.” NASA/TM 2003-104606, Vol. 25, 67 pp.
- Wang, B., 1988: Dynamics of tropical low-frequency waves: An analysis of the moist Kelvin wave. *J. Atmos. Sci.*, **45**, 2051–2065.
- , 2005: Theory. *Intraseasonal Variability in the Atmosphere–Ocean Climate System*, W. K.-M. Lau and D. E. Waliser, Eds., Praxis, 307–360.
- , and H. Rui, 1990: Dynamics of the coupled moist Kelvin–Rossby wave on an equatorial β -plane. *J. Atmos. Sci.*, **47**, 397–413.
- , and T. Li, 1994: Convective interaction with boundary-layer dynamics in the development of a tropical intraseasonal system. *J. Atmos. Sci.*, **51**, 1386–1400.
- , and X. Xie, 1997: A model for the boreal summer intraseasonal oscillation. *J. Atmos. Sci.*, **54**, 72–86.
- , and —, 1998: Coupled modes of the warm pool climate system. Part I: The role of air–sea interaction in maintaining Madden–Julian oscillation. *J. Climate*, **11**, 2116–2135.
- , and F. Liu, 2011: A model for scale interaction in the Madden–Julian oscillation. *J. Atmos. Sci.*, **68**, 2524–2536.
- Wheeler, M., and G. N. Kiladis, 1999: Convectively coupled equatorial waves: Analysis of clouds and temperature in the wavenumber–frequency domain. *J. Atmos. Sci.*, **56**, 374–399.
- Xie, X., and B. Wang, 1996: Low-frequency equatorial waves in vertically sheared zonal flow. Part II: Unstable waves. *J. Atmos. Sci.*, **53**, 3589–3605.
- Zhang, C., 2005: Madden–Julian oscillation. *Rev. Geophys.*, **43**, RG2003, doi:10.1029/2004RG000158.